Synthesis, crystal structure, molecular orbital calculations and electronic properties of 2,3-di(2-pyridyl)naphtho[2,3-*f*]quinoxaline-7,12-quinone (Aqdpp)

Rosa López,[a] Daphne Boys,[b] Bárbara Loeb *,[a] and Fernando Zuloaga *,[a]

[a] *Facultad de Quimica, Pontificia Universidad Catolica de Chile, Casilla 306, Santiago, Chile*
[b] *Departamento de Fisica, Facultad de Ciencias Fisicas y Matematicas, Universidad de Chile, Casilla 487-3, Santiago, Chile*

The synthesis, characterization and crystal structure of 2,3-di(2-pyridyl)naphtho[2,3-*f*]quinoxaline-7,12-quinone (Aqdpp) are reported. Molecular orbital calculations have been carried out in order to characterize its reactivity and coordination properties. Surface maps for the electronegativity, hardness and Fukui functions have been generated to identify local reactivity sites and the crystal structure has been compared with the optimized geometry with good correlation among them. The acceptor properties of the Aqdpp ligand are shown by the orbital map for the LUMO level contributed mainly by the quinonic region of the ligand.

Introduction

Interest in d^6 complexes of Ru^{II}, Os^{II} and Re^{I} has increased in recent years due to their ability to act as photosensitizers in photoinduced electron and energy transfer processes.[1] The properties of this type of complex are strongly influenced by the nature of the chelating ligand. Polypyridyl ligands, like bpy (2,2′-bipyridine) or phen (1,10-phenanthroline) have been widely used. By appropriate derivatization these types of ligands can behave as electron donors or electron acceptors.[2] Aiming to design bidentate chelating ligands with a strong acceptor capacity, we have started to synthesise ligands which incorporate quinonic groups in non-coordinating positions.[3] In this paper we report the preparation, characterization and crystal structure of 2,3-di(2-pyridyl)naphtho[2,3-*f*]quinoxaline-7,12-quinone, Aqdpp, shown in Fig. 1, where [A] denotes the anthraquinone plus diazine ring moiety.

Molecular orbital calculations have also been carried out to characterize the reactivity of this ligand molecule. In order to achieve this goal, suitable relations derived from density functional theory (DFT)[4] like the chemical potential μ or the molecular electronegativity χ, the hardness η and the electrostatic potential $\varphi(\boldsymbol{r})$ at a point $\boldsymbol{r}$ in the molecule, are used. The basic relations are given in eqns. (1) and (2), where E is the

$$\chi = -\left(\frac{\delta E}{\delta N}\right)_v \tag{1}$$

$$\eta = \frac{1}{2}\left(\frac{\delta^2 E}{\delta N^2}\right)_v \tag{2}$$

electronic energy, N the number of electrons and v the external potential due to the nuclei. χ is not a simple function of the state of the system. Instead, it depends on whether the system can only lose electrons ($\chi = E_i$, the ionization potential) or can only gain electrons ($\chi = E_{ea}$, the electron affinity). When dealing with molecular systems for which both gain and loss of electrons are allowed, finite approximations for electronegativity χ and hardness η are frequently used[5] [eqns. (3) and (4)].

$$\chi = \frac{E_i + E_{ea}}{2} \tag{3}$$

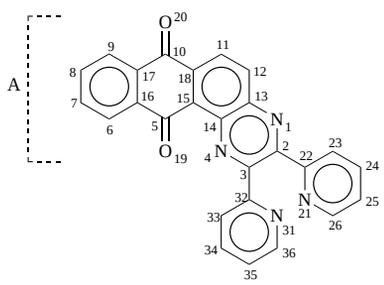

Fig. 1 Planar skeleton for the molecule Aqdpp. The anthraquinone-diazine rings molecular region is denoted by [A].

$$\eta = \frac{E_i - E_{ea}}{2} \tag{4}$$

In this paper the molecular electrostatic potential, electronegativity and electron density distribution are used to evaluate the electron acceptor and chelation ligand capacity of Aqdpp. Additionally, maps for local site chemical hardness derived from the electrostatic potential are obtained for the first time for a molecule. The optimized molecular geometry for Aqdpp is compared with the crystal structure in the solid state, and conclusions are drawn regarding the possible configuration of the molecule in solution and its reactivity.

Experimental

Physical measurements

UV–VIS spectra were recorded on a Milton Roy 3000 diode array spectrometer. ^{1}H NMR spectra were recorded on a Bruker AC/200, 200 MHz spectrometer with TMS as reference. Cyclic voltammetry was performed using a Wenking HP 72 potentiostat, a Wenking VSG 72 signal generator and a Graphtex WX 2300 recorder. A platinum disk was used as the working electrode. The counter electrode was a platinum wire and the reference electrode was a Ag/AgCl (in aqueous tetramethyl ammonium chloride), calibrated to SCE. All potentials are reported relative to SCE. Dichloroethane (DCE) was used as solvent, and was freshly distilled before each measurement. Tetrabutylammonium tetrafluoroborate 0.1 M was used as supporting electolyte. IR spectra were recorded in KBr mulls in a Bruker Vector 22 FTIR spectrometer.

Materials

All chemicals were reagent grade and used as received. 1,2-Di(2-pyridyl)ethane-1,2-dione (2,2′-pyridyl) and 1,2-diaminoanthraquinone were obtained from Aldrich.

Synthesis of 2,3-di(2-pyridyl)naphtho[2,3-*f*]quinoxaline-7,12-quinone, Aqdpp

0.480 g (2.086 mmol) of 1,2-diaminoanthraquinone and 0.420 g (2.086 mmol) of 1,2-di(2-pyridyl)ethane-1,2-dione were dissolved in 50 ml ethanol. The mixture was refluxed for 4 days. The solvent was eliminated by evaporation and the red residue dissolved in chloroform. After heating, the solution was treated twice with active charcoal, filtered and concentrated until an orange colored solid started to precipitate. The precipitation was completed by the addition of diethyl ether. The product was washed repeatedly with diethyl ether and dried under high vacuum. The single crystals for X-ray structure determination were obtained by slow evaporation of a solution of the compound in chloroform. Elemental analysis gave satisfactory results. Yield: 86.8%. ν_{max}(KBr)/cm^{-1} 1598 (CN) and 1672 (C=O); λ_{max}($CHCl_3$)/nm 384 and 266; δ_H($CDCl_3$, assigned with the aid of ^{1}H COSY) 8.73 [H(11), d], 8.58 [H(36), d], 8.55 [H(12), d], 8.43 [H(26), d], 8.32 [H(9), m], 8.1 [H(6), m], 7.8–7.9 [H(34), H(24), H(8), m], 7.2–7.4 [H(35), H(25), H(7), m]; $E_{0,1/2}$ (red) = −0.64; −0.86 V (in DCE).

Crystal structure determination

A suitable single crystal, grown from $CHCl_3$ by slow evaporation was used for the X-ray data collection.†

Crystal data. $C_{26}H_{14}N_4O_2$, M = 414.4, Monoclinic, a = 8.514(2), b = 25.237(6), c = 9.431(2) Å, V = 1898.3(7) Å^3, by least-squares fit of 25 centered reflections with $5 < \theta < 15°$, λ(Mo-Kα) = 0.710 73 Å, space group $P2_1/n$ (alt. $P2_1/c$, No. 14), Z = 4, D_x = 1.450 Mg m^{-3}; dark orange tablet of approximate dimensions 0.32 × 0.14 × 0.36 mm, μ(Mo-Kα) = 0.095 mm^{-1}.

Data collection and processing. Siemens R3m/V diffractometer, $\omega/2\theta$ scan mode with graphite-monochromated Mo-K$_\alpha$ radiation; 3750 reflections collected with $1.5 < \theta < 25°$ (h: 0→10, k: 0→30; l: −11→10), 3342 unique (R_{int} = 5.98%), 1492 with $F > 3.0\sigma(F)$; 2 standard reflections monitored every 98 reflections revealed no significant intensity variation. Semi-empirical absorption correction, *via* psi scans (max., min. transmission factors = 0.9491, 0.9257).

Structure analysis and refinement. The structure was solved using direct methods and refined on F by full-matrix least-squares procedures, with all non-hydrogen atoms anisotropic. Hydrogens, at calculated positions, were allowed to ride on parent carbon atoms with bond distances equal to 0.96 Å and isotropic U equal to 1.2 times the equivalent isotropic U of the attached carbon atom. Correction for extinction, and weighting scheme $w^{-1} = \sigma^2(F) + 0.0002F^2$. Final $R = \Sigma\Delta/\Sigma F_o$ where $\Delta = |F_o - F_c|$ and $R_w = \Sigma\Delta\sqrt{w}/\Sigma F_o\sqrt{w}$ values, for observed reflections, are 0.043 and 0.037 respectively. All calculations were performed with the Siemens SHELXTL-Plus system of programs (PC version).[6]

Theoretical and computational details

The frontier molecular orbital (FMO) calculations and full geometry optimization for Aqdpp were carried out using PM3 methods[7] implemented in the Spartan package.[8] Molecular calculations were also generated by density functional theory (DFT) methods[4] with Becke exchange and Lee–Yang–Parr correlation potentials (BLYP)[7,9] to evaluate the total energy, the ionization energy and the electron affinity from total energy differences between ionic and neutral molecules, with the electronic chemical potential related to the electronegativity by[5] $-\mu = \chi$.

The molecular electrostatic potential provides information about preferential reactivity sites in molecules not only towards electrophiles but also towards nucleophiles, by plotting its surface.[10] The electrostatic potential $\varphi(\boldsymbol{r})$ that the electrons and nuclei of a molecule create at each point $\boldsymbol{r}$ in the surrounding space is given rigorously by eqn. (5), where Z_A is the charge on

$$\varphi(\boldsymbol{r}) = \sum_A \frac{Z_A}{|\boldsymbol{R}_A - \boldsymbol{r}|} - \int \frac{\rho(\boldsymbol{r}')\,d\boldsymbol{r}'}{|\boldsymbol{r}' - \boldsymbol{r}|} \quad (5)$$

nucleus A located at $\boldsymbol{R}_A$, and $\rho(\boldsymbol{r})$ is the electronic density function of the molecule for the occupied molecular orbitals $\psi_i(\boldsymbol{r})$ with occupation number n_i [eqn. (6)].

$$\rho(\boldsymbol{r}) = \sum_{i=1}^{occ} n_i|\psi_i(\boldsymbol{r})|^2 \quad (6)$$

Interestingly, $\varphi(\boldsymbol{r})$ is a real physical property that can be calculated theoretically or derived from diffraction experiments. Thus, any molecular reactivity index derived from it will also correspond to useful experimental parameters.

The isosurface for the electrostatic potential and the electronegativity surface map for the molecule were drawn following a similar principle already applied for atoms:[11] the electrostatic potential is directly related to the electronegativity in a molecular system[4] *via* eqn. (7), where $T_s(\rho)$ and $E_{xc}(\rho)$ are the

$$\chi = -\frac{\delta T_s(\rho)}{\delta\rho(\boldsymbol{r})} + \varphi(\boldsymbol{r}) - \frac{\delta E_{xc}(\rho)}{\delta\rho(\boldsymbol{r})} \quad (7)$$

Kohn–Sham non-interacting single particle kinetic energy and the exchange-correlation energy, respectively. Since the electronegativity is constant throughout the molecular space eqn. (7) suggests that it is possible to find a set of $\boldsymbol{r}_\chi$ values at which the equality[11] [eqn. (8)] holds so that $\chi = \varphi(\boldsymbol{r}_\chi)$. According to

$$-\frac{\delta T_s(\rho)}{\delta\rho(\boldsymbol{r}_\chi)} = \frac{\delta E_{xc}(\rho)}{\delta\rho(\boldsymbol{r}_\chi)} \quad (8)$$

eqns. (1) and (3) this requires that the ionization potential E_i and the electronaffinity E_{ea} are also present in the $\varphi(\boldsymbol{r}_{E_i})$ and $\varphi(\boldsymbol{r}_{E_{ea}})$ surfaces, respectively. Thus, the surface drawn with the restriction for $\varphi(\boldsymbol{r}_\chi)$, the value of which is a known molecular electronegativity value, yields the electronegativity surface map for the molecule that encloses all its atoms [eqn. (9)].

$$\chi = \sum_A \frac{Z_A}{|\boldsymbol{R}_A - \boldsymbol{r}|} - \int \frac{\rho(\boldsymbol{r}')\,d\boldsymbol{r}'}{|\boldsymbol{r}' - \boldsymbol{r}|}; \quad \boldsymbol{r} = \{\boldsymbol{r}_\chi\} \quad (9)$$

In addition, from the derivatives $(\delta\boldsymbol{r}_\chi/\delta N)_v = [\delta\varphi(\boldsymbol{r}_\chi)/\delta N]_v = 2\eta(\boldsymbol{r}_\chi)$, molecular hardness plots at $\{\boldsymbol{r}_\chi\}$ were obtained. Two possible phenomena were analyzed: an electrophilic attack over the molecule (thereby the HOMO is involved for the δN electron transfer process), [eqn. (10)], and a nucleophilic attack (LUMO

$$2\eta_-(\boldsymbol{r}_\chi) = \int \frac{\rho_{HOMO}(\boldsymbol{r}')\,d\boldsymbol{r}'}{|\boldsymbol{r}' - \boldsymbol{r}_\chi|} \quad (10)$$

involved) [eqn. (11)]. Since $\rho(\boldsymbol{r})$ contains the information for the occupied levels it was only necessary to build a new charge

$$2\eta_+(\boldsymbol{r}_\chi) = \int \frac{\rho_{LUMO}(\boldsymbol{r}')\,d\boldsymbol{r}'}{|\boldsymbol{r}' - \boldsymbol{r}_\chi|} \quad (11)$$

† Full crystallographic details, excluding structure factor tables, have been deposited at the Cambridge Crystallographic Data Centre (CCDC). For details of the deposition scheme, see 'Instructions for Authors', *J. Chem. Soc., Perkin Trans. 2*, available *via* the RSC Web page (http://www.rsc.org/authors). Any request to the CCDC for this material should quote the full literature citation and the reference number 188/124.

density for the negative ion molecule at the ground state configuration of the neutral molecule.

Eqns. (10) and (11) establish that the frontier orbital electrostatic potential at different values of r_χ is a measure of the hardness achieved by the molecule in response to a perturbation represented by the electrophile or nucleophile, respectively. By this procedure a contour surface for η encoded to χ was built around the molecule to learn which site yields the hardest molecular value for a given chemical attack. This statement conforms with the maximum hardness principle already stated[12] that has been used to explain stability in cluster formation,[13] to deduce the orientation of electrophilic aromatic substitution[14] and to determine regiospecificity in Diels–Alder reactions:[15] 'the molecular system will prefer to react against external perturbations as to acquire the highest possible hardness.'

Finally, eqns. (10) and (11) are of the form[16] given in eqn. (12),

$$\eta_{\pm}(\boldsymbol{r}_\chi) = \int \eta(\boldsymbol{r}, \boldsymbol{r}_\chi) f_{\pm}(\boldsymbol{r}) d\boldsymbol{r} \qquad (12)$$

where $f(\boldsymbol{r}) = [\delta\rho(\boldsymbol{r})/\delta N]_v$ is the Fukui function previously proved to be useful for discussing reactivity.[17] Therefore, $f_-(\boldsymbol{r}) = \rho_{HOMO}(\boldsymbol{r})$ for electrophilic attack and $f_+(\boldsymbol{r}) = \rho_{LUMO}(\boldsymbol{r})$ for nucleophilic attack as stated elsewhere.[18]

Results and discussion

The synthesis of Aqdpp was carried out by a condensation reaction, comparable to that reported for similar compounds[3] (Scheme 1). The condensation was verified by the disappear-

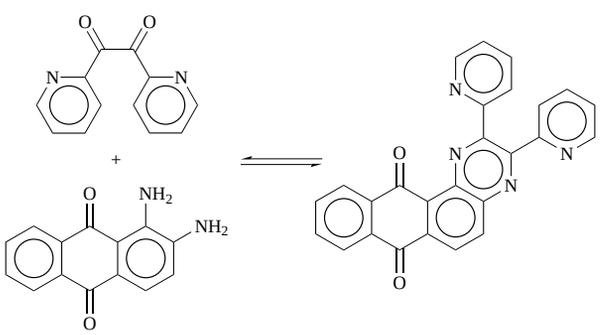

Scheme 1

ance of the carbonyl tension bands of 1,2-di(2-pyridyl)ethane-1,2-dione (1713 and 1691 cm^{-1}) and NH tensions of 1,2-diaminoanthraquinone (3500 cm^{-1}). Further characterization was achieved by ^1H NMR spectroscopy. Fig. 2 shows the ^1H COSY spectra for Aqdpp where the great number of signals observed demonstrates the inequivalency of the pyridyl ring protons. On the other hand, the complexity of the multiplets between 7.8–7.9 and 7.2–7.4 ppm shows the mixing of some of the pyridyl ring protons with the AA′BB′ system of the anthraquinone fragment. The UV–VIS absorption spectrum is dominated by the characteristic anthraquinone bands, in the region 380–400 nm.[19] The acceptor properties of the ligand were evidenced by cyclic voltammetry, where two reductions occurred. The first (−0.64 V) is reversible, and was attributed to the formation of the semiquinone, while the second (−0.86 V) is irreversible and probably related to the formation of the dianion. These assignments are supported by EPR measurements on the similar ligand 12,17-dihydronaphtho[2,3-*h*]dipyrido[3,2-*a*:2′,3′-*c*]phenazine-12,17-dione,† Aqphen,[3] where the formation of the semiquinone by one electron reduction was clearly established.[20]

† In a previous paper (ref. 3) the name used for Aqphen was 10,11-[1,4-napthalenedione]dipyrido[3,2-*a*:2″,3′-*c*]phenazine.

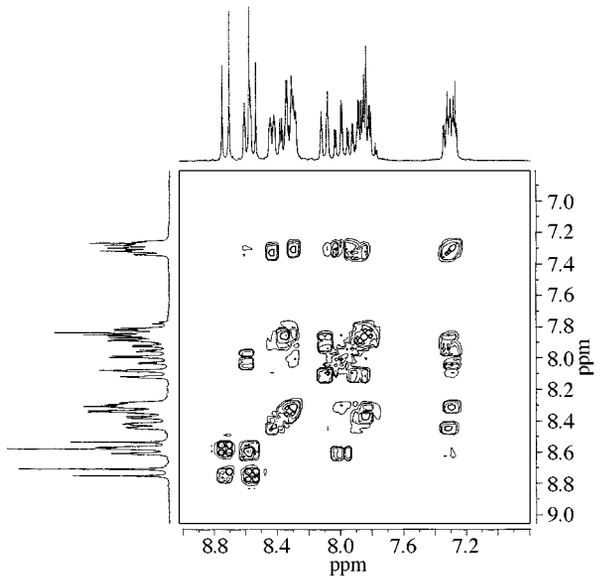

Fig. 2 ^1H COSY spectrum for Aqdpp, in $CDCl_3$

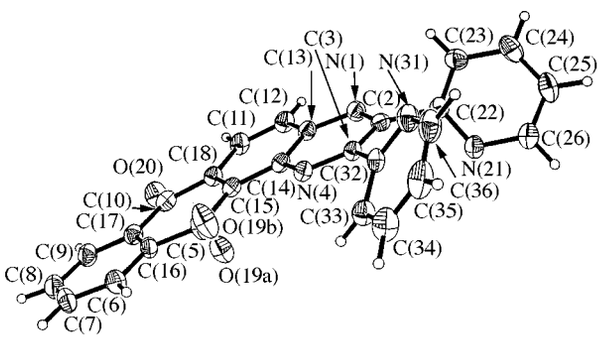

Fig. 3 ORTEP plot for Aqdpp. Thermal ellipsoids drawn at 30% probability level.

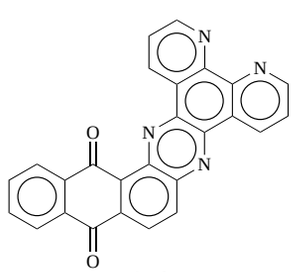

Aqphen

Fig. 3 shows an ORTEP plot of the structure of the Aqdpp ligand in the crystalline state as determined by X-ray diffraction. All bond distances and angles are within normal values. Special mention must be made of the anomalous behavior exhibited by atom O(19)—during refinement of structure—which was manifested through an extremely high anisotropic coefficient. The behavior of this oxygen atom was best modeled assuming positional disorder with occupation factors of 0.70 and 0.30 [O(19a) and O(19b) respectively, see Table 1]. The anthraquinone-diazine entity is quite planar with a maximum deviation of 0.138(4) Å from the best mean plane. The pyridine groups, on the other hand, are oriented out of plane with dihedral angles of 57.0(2)° between each other and angles of 132.8(1) and 144.4(2)° with respect to the pyrazine ring. In the crystal, close molecules pack with their planar skeletons parallel to each other, while neighboring adjacent molecules, related by the center of symmetry, exhibit close contacts between atoms C(6) and O(19b) [C(6)–H(6)···O(19b) = 3.121(23) Å].

In order to gain an insight into the preferred structure of the ligand in solution and into its preferential reactivity and coordination sites, theoretical calculations as described in the

Table 1 Selected interatomic bond distances (Å) for Aqdpp. Estimated standard deviations for the observed least significant figure are given in parentheses.

Bond	Observed	Calculated
C(10)–C(18)	1.493(5)	1.495
C(10)–C(17)	1.479(5)	1.490
C(10)–O(20)	1.219(5)	1.216
C(18)–C(15)	1.388(6)	1.384
C(18)–C(11)	1.405(5)	1.414
C(15)–C(5)	1.496(5)	1.496
C(15)–C(14)	1.428(5)	1.422
C(5)–C(16)	1.483(5)	1.493
C(5)–O(19a,b)	1.251(10), 1.248(25)	1.212
C(16)–C(6)	1.385(5)	1.391
C(16)–C(17)	1.397(6)	1.402
C(6)–C(7)	1.381(5)	1.393
C(7)–C(8)	1.386(6)	1.395
C(8)–C(9)	1.382(6)	1.393
C(9)–C(17)	1.392(5)	1.392
C(13)–C(14)	1.413(5)	1.415
C(13)–N(1)	1.367(4)	1.396
C(13)–C(12)	1.405(6)	1.416
C(14)–N(4)	1.362(5)	1.393
N(1)–C(2)	1.321(5)	1.327
C(12)–C(11)	1.362(5)	1.373
C(3)–C(32)	1.481(6)	1.481
C(3)–N(4)	1.314(4)	1.327
C(3)–C(2)	1.428(5)	1.446
C(32)–N(31)	1.340(6)	1.360
C(32)–C(33)	1.387(5)	1.398
C(2)–C(22)	1.496(5)	1.481
C(22)–C(23)	1.375(5)	1.398
C(22)–N(21)	1.350(5)	1.361
N(31)–C(36)	1.339(6)	1.350
C(33)–C(34)	1.380(6)	1.393
C(34)–C(35)	1.370(8)	1.390
C(23)–C(24)	1.386(6)	1.393
C(36)–C(35)	1.385(6)	1.397
N(21)–C(26)	1.343(5)	1.350
C(26)–C(25)	1.388(5)	1.397
C(24)–C(25)	1.375(6)	1.390

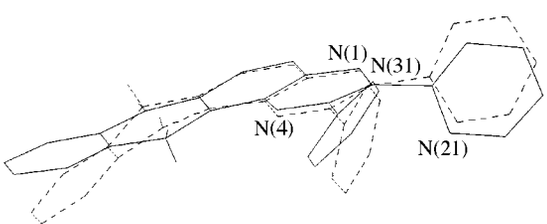

Fig. 4 Comparison of crystal structure and optimized molecular geometry for Aqdpp. Full lines correspond to the crystalline structure and dotted lines to the calculated structure.

previous section were performed. First, the optimized molecular geometry was calculated and compared to the crystallographical one, as shown in Fig. 4. Bond distances, bond angles and torsion angles are given in Tables 1, 2 and 3, respectively. Both X-ray and theoretical optimization methods agree quite well regarding the stereochemical orientation for the pyridyl rings of Fig. 1, with the N atoms located above and below the molecular plane defined by the pyrazine ring. Moreover, bond distance and bond angle data also show that the gas phase optimized geometry for this molecule compares well with the molecular geometry in the crystalline state, with the exceptions of minor details around the pyridyl groups and strong distortions on the quinone ring. For example, both structures show that the −C=O groups are out of plane, specially C(5)–O(19) for which the crystallographic value shows a positional disorder. The full anthraquinone part of this ligand molecule is bent at the central ring with a distortion angle of 35.8° for the calculated molecule in the gas phase. This bending is higher than the

Table 2 Selected interatomic bond angles (°) for Aqdpp. Estimated standard deviations for the observed least significant figure are given in parentheses.

Angle	Observed	Calculated
C(18)–C(10)–C(17)	117.7(4)	114.2
C(18)–C(10)–O(20)	121.1(3)	122.8
C(17)–C(10)–O(20)	121.2(3)	123.0
C(10)–C(18)–C(15)	122.4(3)	119.9
C(10)–C(18)–C(11)	116.6(4)	118.9
C(15)–C(18)–C(11)	121.0(3)	121.2
C(18)–C(15)–C(5)	119.2(3)	118.0
C(18)–C(15)–C(14)	118.3(3)	118.8
C(5)–C(15)–C(14)	122.5(3)	123.2
C(15)–C(5)–C(16)	118.4(3)	113.7
C(15)–C(5)–O(19a,b)	122.0(5), 116.1(9)	124.0
C(16)–C(5)–O(19a,b)	118.5(5), 117.9(10)	122.3
C(5)–C(16)–C(6)	118.9(4)	121.3
C(5)–C(16)–C(17)	121.6(3)	118.5
C(6)–C(16)–C(17)	119.5(3)	120.1
C(10)–C(17)–C(16)	120.3(3)	118.8
C(10)–C(17)–C(9)	119.8(4)	121.3
C(16)–C(17)–C(9)	119.9(3)	119.9
C(32)–C(3)–N(4)	114.5(3)	117.2
C(32)–C(3)–C(2)	123.8(3)	122.2
C(3)–C(32)–N(31)	118.1(3)	117.4
C(3)–C(32)–C(33)	118.9(4)	121.1
N(1)–C(2)–C(22)	114.7(3)	117.4
C(3)–C(2)–C(22)	124.3(3)	122.1
C(2)–C(22)–C(23)	121.3(3)	121.2
C(2)–C(22)–N(21)	115.0(3)	117.1

Table 3 Selected torsion angles (°) for Aqdpp. Estimated standard deviations for the observed least significant figure are given in parentheses.

Angle	Observed	Calculated
C(17)–C(10)–C(18)–C(15)	6.8(6)	−19.7
C(17)–C(10)–C(18)–C(11)	−175.6(4)	159.9
O(20)–C(10)–C(18)–C(15)	−172.5(4)	162.4
O(20)–C(10)–C(18)–C(11)	5.2(6)	−18.0
C(18)–C(10)–C(17)–C(16)	−6.0(6)	21.1
C(18)–C(10)–C(17)–C(9)	175.5(4)	−158.8
O(20)–C(10)–C(17)–C(16)	173.2(4)	−161.0
O(20)–C(10)–C(17)–C(9)	−5.3(7)	19.1
C(10)–C(18)–C(15)–C(5)	−1.5(6)	−5.8
C(10)–C(18)–C(15)–C(14)	176.7(4)	175.6
C(18)–C(15)–C(5)–C(16)	−4.4(6)	29.0
C(18)–C(15)–C(5)–O(19a,b)	163.4(4), −153.4(12)	−148.1
C(14)–C(15)–C(5)–O(19a,b)	−14.6(9), 28.6(13)	30.7
C(15)–C(5)–C(16)–C(17)	5.1(7)	−27.6
O(19a,b)–C(5)–C(16)–C(6)	16.5(8), −26.8(12)	−28.3
O(19a,b)–C(5)–C(16)–C(17)	−163.2(7), 153.5(11)	149.6
C(5)–C(16)–C(17)–C(10)	0.2(7)	2.6
C(8)–C(9)–C(17)–C(10)	−178.4(4)	178.9
C(13)–N(1)–C(2)–C(22)	169.8(4)	179.7
N(4)–C(3)–C(32)–N(31)	−142.2(4)	−126.0
N(4)–C(3)–C(32)–C(33)	35.2(6)	53.3
C(2)–C(3)–C(32)–N(31)	36.8(6)	53.9
C(2)–C(3)–C(32)–C(33)	−145.7(4)	−126.8
C(32)–C(3)–C(2)–C(22)	12.8(7)	0.5
C(3)–C(32)–C(33)–C(34)	−178.4(4)	−179.7
N(1)–C(2)–C(22)–C(23)	44.3(6)	57.5
N(1)–C(2)–C(22)–N(21)	−131.6(4)	−122.0
C(3)–C(2)–C(22)–C(23)	−139.9(5)	−123.3
C(3)–C(2)–C(22)–N(21)	44.2(6)	57.3
C(2)–C(22)–C(23)–C(24)	−176.1(4)	−179.9
C(2)–C(22)–N(21)–C(26)	175.6(4)	179.7

observed one from the crystal structure, and, obviously, they do not have to be the same largely due to the different reference points for the total energy, that is, the gas phase molecule against the crystal packed molecule in the solid phase. The latter shows that the quinone ring, although with some deviations, is close to planar (distortion angle ≈ 4.4°).

Other important points emerge from the comparison of these

Table 4 Electronic structure of Aqdpp

Property	Value
HOMO orbital energy/eV	−9.754
LUMO orbital energy/eV	−1.552
Ionization potential, E_i/eV	7.510[a]
Electron affinity, E_{ea}/eV	2.411[a]
Molecular electronegativity, χ/eV	4.961
Molecular hardness, η/V	2.549
Dipole moment, μ/Debye	3.635

[a] Difference of total DFT energies between neutral and ionic species.

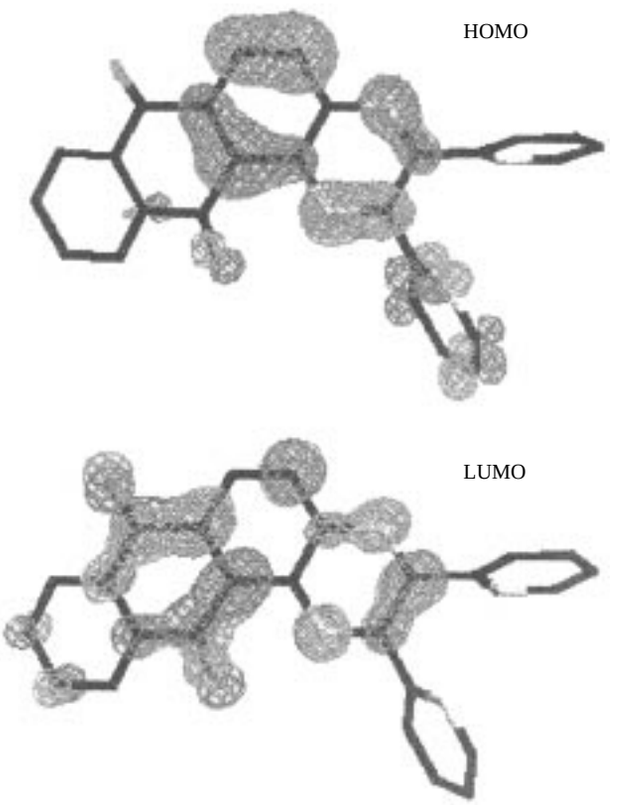

Fig. 5 Molecular surface of the HOMO and LUMO for Aqdpp. The isosurface value is 0.032 e au^{-3}.

results. First, the theoretical results show that the pyridyl groups are twisted out of the molecular diazine ring plane, by 57 and 54° respectively, and both pyridyl planes are not parallel to each other but form an angle close to 49°. The corresponding values for the crystallographic results are 44 and 36° out of the diazine ring plane and approximately 57° for the angle between the pyridyl planes. Thus, as expected, the free pyridyl rings are strongly out of plane. These results suggest that in solution there should exist a higher degree of bending than in the solid phase for this molecule.

Aqdpp also shows a rather peculiar electronic structure. A selection of calculated data are given in Table 4. To begin with, its frontier HOMO and LUMO orbitals shown in Fig. 5 are dominated by the [A] region already defined in Fig. 1. The difference is seen in the magnitude and sign of the orbital coefficients of both frontier orbitals. The [A] region holds almost 95% of the electronic charge (fitted from the electrostatic potential for the neutral and for the singly ionized molecule) for the HOMO level, whereas for the LUMO level it holds 98%. Specifically, within the region [A] the pyrazine ring together with its neighboring benzene ring from the anthraquinone moiety dominates the behaviour for the HOMO level and only one of the free rotating pyridyl rings shows some contribution to it. However, differences are observed when considering the LUMO level where most of the charge distribution has moved up to the anthraquinone group and its adjacent pyrazine ring, with practically no contributions from the pyridyl groups. Thus, pyridyl rings do not seem to play an important role in the frontier orbital description of reactivity for Aqdpp. Under this scheme, it should be emphasized that quinone groups are not significant in the HOMO description whereas for the LUMO its contribution is notable.

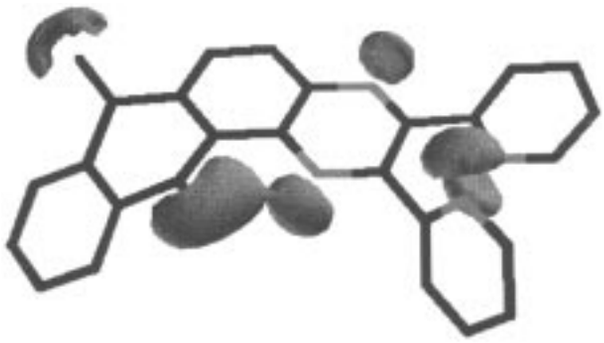

Fig. 6 Molecular electrostatic potential for Aqdpp. The isosurface value is −60 kcal mol^{-1}.

We can learn about the capacity of Aqdpp to coordinate to positive metal ions by investigating the most negative local values of the molecular electrostatic potential $\varphi(\boldsymbol{r})$ given in eqn. (5). By definition, this potential will give rise to an attractive force at a given position $\boldsymbol{r}$ for a unit positive charge located at that position. Fig. 6 shows the resulting isosurface for the electrostatic potential at the value of −60 kcal mol^{-1}. It can be seen that a positive ion could, in principle, become trapped nearby the pyridyl N atoms. The N atoms from the pyrazine ring and the quinone −C=O groups are possible coordination centers as well. It remains to predict which pair of atoms [N(1) and N(21), N(4) and N(31) or N(21) and N(31)] are involved when Aqdpp behaves as a bidentate ligand.

It is important to realize at this point that the electrostatic map at −60 kcal mol^{-1} is not directly related to the molecular electronegativity χ since, by definition, χ is a unique property in any given region of the molecule.[21] A plot of the electrostatic potential of eqn. (9) at the 114.398 kcal mol^{-1} isosurface value (electronegativity value) is shown in Fig. 7. The isosurface surrounds the whole molecule and it does not provide us with enough criteria to assess preferential reactivity sites. It is the hardness function $\eta_+(\boldsymbol{r}_\chi)$ of eqn. (10) for the electrophilic attack [or $\eta_-(\boldsymbol{r}_\chi)$ of eqn. (11) for the nucleophilic attack] together with the principle of maximum hardness that helps us to decide on this matter.[12–15]

Accordingly, in Fig. 7 we have encoded the $\eta_+(\boldsymbol{r}_\chi)$ and $\eta_-(\boldsymbol{r}_\chi)$ hardness local functions on the corresponding molecular isosurface of the electronegativity discussed above. Thus, Aqdpp indeed shows sites with characteristic hardness values for chemical attack. The preferred sites for the electrophilic substitution are C(15) and C(11), the pyrazine ring shows weaker reacting sites and the pyridyl rings are not hard enough to compete for the chemical reactivity towards electrophiles. It is also seen that nucleophilic substitution reactions may occur mainly at C(15), though C(18) is also active.

The molecular Fukui function also provides us with the appropriate tools to determine a specific site for chemical reactivity towards nucleophiles or electrophiles.[17,18] For Aqdpp a plot of f_- and f_+ for electrophilic and nucleophilic attack, respectively, encoded to the charge density at the isosurface value of 0.012 e bohr^{-3} is shown in Fig. 8. These results show the same pattern already discussed in terms of hardness in Fig. 7. In any case, hardness plots seem to be more useful and specific than the Fukui functions for reactivity studies.

The preceding results explain the main features of the chemical reactivity of Aqdpp in substitution reactions. It is found that hardness η_+ values from Fig. 7 together with the principle of maximum hardness[12–14] also provides an explanation for

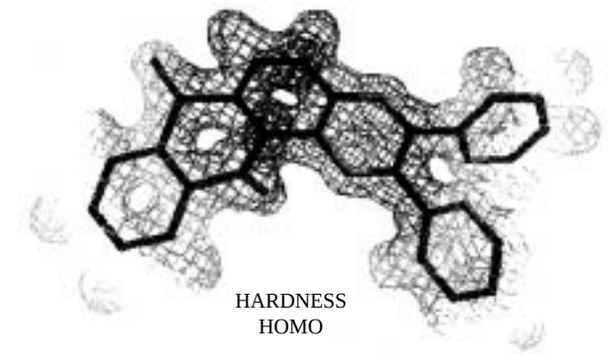

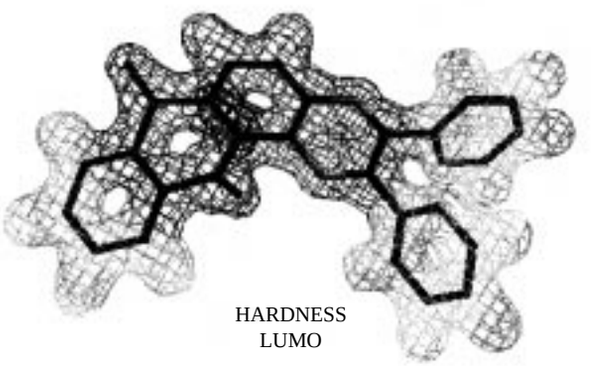

Fig. 7 Electronegativity plot at the isosurface value of 114.398 kcal mol^{-1} with encoded values of local hardness of the HOMO [$\eta_+(\boldsymbol{r}_\chi)$] for electrophilic attack and the LUMO [$\eta_-(\boldsymbol{r}_\chi)$] for nucleophilic attack. The darkest sites are the hardest ones.

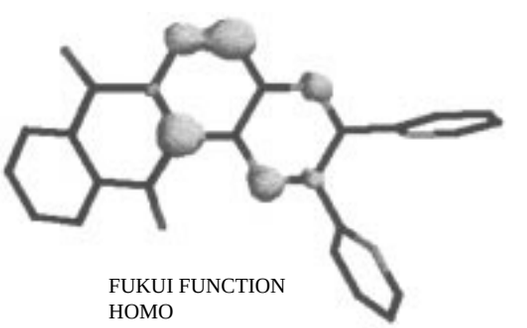

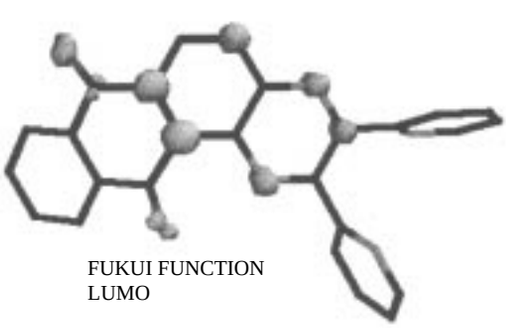

Fig. 8 Fukui function plot at the isosurface value of 0.008 e $bohr^{-3}$ for the HOMO (f_-), and for LUMO (f_+)

the chelating specificity towards positive ions located at the negative values for the electrostatic potential of Fig. 6. Thus, one finds that N(4) ($2\eta_- = 142$ kcal mol^{-1}) is the hardest molecular site compared to N(1) ($2\eta_- = 128.6$ kcal mol^{-1}), N(31) ($2\eta_- = 80$ kcal mol^{-1}) and N(21) ($\eta_- = 64$ kcal mol^{-1}). Furthermore, to corroborate these findings, we have performed a semiempirical PM3 calculation for the complex $AqdppZn^{+2}(H_2O)_2$ with the positive ion coordinated in a monodentate fashion to N(1) ($E_{tot} = -5188.4879$ eV), to N(4) ($E_{tot} = -5188.8889$ eV), to N(21) ($E_{tot} = -5188.818\,99$ eV) and to N(31) ($E_{tot} = -5188.8199$ eV). We also performed similar calculations with the positive ion coordinated in a bidentate fashion to N(4)–N(31) ($E_{tot} = -5188.591\,57$ eV), to N(21)–N(31) ($E_{tot} = -5188.7804$ eV) and to N(1)–N(21) ($E_{tot} = -5188.0470$ eV). Accordingly, these semiempirical results are clearly in favor of the N(1) site for monodentate coordination but make it difficult to decide which bidentate site is the most favored. However, hardness values clearly show that N(4)–N(31) is the preferred choice though both possibilities exist. These findings correlate well with experimental results for the coordination of the dpp residue (pyrazine plus pyridyl rings) reported to form monomers and dimers through bidentate chelation of one pyrazine nitrogen and one pyridyl nitrogen[22] and with preliminary results for an Aqdpp rhenium complex

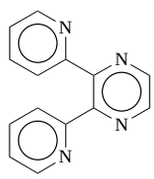

dpp

synthesized in our laboratory where the N(21)–N(31) bidentate coordinating site was inferred from NMR data.[23]

Conclusions

In this paper we have characterized the Aqdpp ligand by means of different experimental and theoretical methods to learn as much as possible about its stereochemistry, reactivity and coordination properties. The expected acceptor characteristics are evidenced by the orbital map for the LUMO level (see Fig. 5) that shows mainly large contributions to the quinone ring. These findings are in agreement with the experimentally observed redox potential for the reduction of the ligand. The crystallographic geometry conforms surprisingly well with the calculated optimized geometry, in spite of the fact that the latter was found for a gas phase molecule.

Hardness values for the Aqdpp molecule based on the molecular electronegativity together with electrostatic potential values were also calculated as was previously done for atoms.[11] The hardness maps allowed us to identify reactivity patterns and preferred coordination sites based on HSAB theory.

Acknowledgements

We thank Fondecyt-Chile (research grants 1940577 and 1971202) and Conicyt-Chile (research grant 2950063 to R. L.) for financial support. D. B. acknowledges the support of Fundacion Andes. Finally, we thank Dr Ana María Leiva for the NMR interpretation.

References

1 (*a*) T. J. Meyer, *Acc. Chem. Res.*, 1989, **22**, 163; (*b*) T. J. Meyer, in *Photochemical Processes in Organized Molecular Systems*, ed. K. Honda, Elsevier, Amsterdam, 1991, p. 133.
2 (*a*) G. Tapolsky, R. Duesing and T. J. Meyer, *Inorg. Chem.*, 1990, **29**, 2285; (*b*) J. P. Sauvage, J. P. Collin, J. C. Chambron, S. Guillerez, C. Coundret, V. Balzani, F. Barigelleti, L. Della and L. Falmigni, *Chem. Rev.*, 1994, **94**, 993; (*c*) W. Lynne and P. Rillema, *Inorg. Chem.*, 1993, **32**, 3836.
3 R. López, B. Loeb, T. Boussie and T. J. Meyer, *Tetrahedron Lett.*, 1996, **37**, 5437.
4 R. G. Parr and W. Yang, *Density Functional Theory of Atoms and Molecules*, Oxford University Press, New York, 1989.
5 G. Liu and R. G. Parr, *J. Am. Chem. Soc.*, 1995, **117**, 3179 and references therein.
6 G. M. Sheldrick, SHELXTL-Plus, release 4.2 for Siemens Crystallographic Research System, Siemens Analytical X-ray Ray Instruments, Inc., Madison, Wisconsin, USA, 1990.

7 C. Lee, W. Yang and R. G. Parr, *Phys. Rev.*, *Sect. B*, 1988, **37**, 785.
8 SPARTAN, version 4.1, Wavefunction Inc., Von Karman Ave. 370, 18401 Irvine, CA, 1996.
9 A. D. Becke, *Phys. Rev.*, *Sect. A*, 1988, **38**, 3089.
10 P. Sjoberg and P. Politzer, *J. Phys. Chem.*, 1990, **94**, 3959.
11 (*a*) P. Politzer, R. G. Parr and D. R. Murphy, *J. Chem. Phys.*, 1983, **79**, 3859; (*b*) M. K. Harbola, R. G. Parr and C. Lee, *J. Chem. Phys.*, 1991, **94**, 6055.
12 R. G. Pearson, *J. Org. Chem.*, 1989, **96**, 3283; R. G. Pearson and W. E. Palke, *J. Phys. Chem.*, 1992, **96**, 3283; R. G. Pearson, *Acc. Chem. Res.*, 1993, **26**, 250.
13 M. K. Harbola, *Proc. Natl. Acad. Sci. USA*, 1992, **89**, 1036.
14 Z. Zhou and R. G. Parr, *J. Am. Chem. Soc.*, 1990, **112**, 5722.
15 F. Zuloaga, R. Tapia and C. Quintanar, *J. Chem. Soc.*, *Perkin Trans. 2*, 1995, 939.
16 M. Berkowitz and R. G. Parr, *J. Chem. Phys.*, 1988, **88**, 2554.
17 K. Fukui, *Science*, 1987, **218**, 747.
18 W. Yang, R. G. Parr and R. Pucci, *J. Chem. Phys.*, 1984, **81**, 2862.
19 *Absorption Spectra in the Ultraviolet and Visible Region*, ed. L. Lang, Academic Press, New York, 1967, vol. 8.
20 E. Norambuena, R. López and B. Loeb, unpublished work.
21 P. Politzer and H. Weinstein, *J. Chem. Phys.*, 1979, **71**, 4218.
22 B. J. Yoblinski, M. Stathis and T. F. Guarr, *Inorg. Chem.*, 1992, **31**, 5.
23 A. M. Leiva, R. López and B. Loeb, unpublished results.

Paper 7/07858G
Received 31*st October* 1997
Accepted 5*th February* 1998